NANOMATERIALS

Twisted epitaxy of gold nanodisks grown between twisted substrate layers of molybdenum disulfide

Yi Cui[1], Jingyang Wang[1,2], Yanbin Li[1], Yecun Wu[1], Emily Been[1], Zewen Zhang[1], Jiawei Zhou[1], Wenbo Zhang[1], Harold Y. Hwang[1,3]*, Robert Sinclair[1]*, Yi Cui[1,4,5]*

We expand the concept of epitaxy to a regime of "twisted epitaxy" with the epilayer crystal orientation between two substrates influenced by their relative orientation. We annealed nanometer-thick gold (Au) nanoparticles between two substrates of exfoliated hexagonal molybdenum disulfide (MoS_2) with varying orientation of their basal planes with a mutual twist angle ranging from 0° to 60°. Transmission electron microscopy studies show that Au aligns midway between the top and bottom MoS_2 when the twist angle of the bilayer is small (<~7°). For larger twist angles, Au has only a small misorientation with the bottom MoS_2 that varies approximately sinusoidally with twist angle of the bilayer MoS_2. Four-dimensional scanning transmission electron microscopy analysis further reveals a periodic strain variation (<|±0.5%|) in the Au nanodisks associated with the twisted epitaxy, consistent with the Moiré registry of the two MoS_2 twisted layers.

Epitaxy is an important phenomenon in materials science that describes the situation when one crystalline material grows on a substrate with exact crystallographic registry in an ordered manner (*1*, *2*). Epitaxy has been used in synthesizing and fabrication of many materials, including planar semiconductor heterostructures (*3*, *4*) and linear and core-shell nanocrystals (*5*–*8*) and nanowires (*9*–*11*), with applications including transistors (*12*–*15*), light-emitting diodes (*16*–*18*), lasers (*19*–*22*), and quantum devices (*23*–*26*). The recent development of two-dimensional (2D) van der Waals (vdW) materials has expanded the scope of epitaxy to vdW epitaxy (*27*–*30*), remote epitaxy (*31*, *32*), and confined epitaxy (*33*–*35*). Thus far, research has been mainly based on the framework of growing one crystal epitaxially onto or into one substrate. Here, we explore a regime of epitaxy between two twisted substrates, or "twisted epitaxy," in which both substrates interact with the grown crystal epilayer and influence its crystallographic registry. This approach allows the relative orientation of two substrates to be used as a structural control parameter.

We explored 2D vdW materials as substrate candidates because they can easily be stacked mechanically to form nanoscale separations for confining atoms and molecules (*36*, *37*). Although the growth of crystals in nanoscale gaps between graphene vdW materials has been reported, these studies did not examine the influence of both substrates in the twisted epitaxy regime (*38*–*40*). For example, a single layer of β-CuI, which only exists in the 645 to 675 K temperature range, was stabilized at room temperature by graphene encapsulation (*38*), but the orientation of the as-synthesized β-CuI relative to twisted bilayers of graphene was not fully investigated. To fabricate 2D low-melting-point metals, Briggs *et al.* used silicon carbide (SiC) (0001) as a template, with epitaxial graphene (EG) on top instead of bilayer graphene (*35*). Metal atoms (Ga, In, and Sn) were intercalated into the interface of EG and SiC to produce 2D metamaterials of three-atomic-layer thickness. These 2D metals were thought not to be bonded to the top graphene layer but rather covalently bonded to the Si atoms below and thus had epitaxial orientation only with the SiC crystal (*35*).

We propose using 2D molybdenum disulfide (MoS_2) as the two substrates and gold (Au) as the twisted epilayer. The chemical interaction between Au and sulfur (S) atoms is much stronger than conventional vdW interaction but weaker than covalent bonding (*41*, *42*, *43*). This configuration would not only stabilize 2D Au but also tune its orientation. Previous studies of Au through vacuum deposition onto single-crystal MoS_2 have shown that there is an epitaxial relationship between the face-centered cubic (fcc) close-packed Au planes ($\{1\bar{1}1\}$) and the hexagonal MoS_2 planes ({001}) (*30*, *44*). The morphology of Au and the interfacial orientation were determined by transmission electron microscopy (TEM) and selected-area electron diffraction (SAED) patterns. The as-deposited Au exhibits a morphology of 3D nanoislands with a typical size of 20 nm and thickness of 8 nm (Fig. 1A) (*30*, *43*). The ability to synthesize and utilize ultrathin Au by conventional film deposition techniques is limited by its poor wetting characteristics on many surfaces, including MoS_2. For thin layers (nominal thickness of <1 nm), Au epitaxial nanoparticles (NPs) are formed; in effect, the higher surface area favored NPs over a continuous film. In the epitaxial MoS_2-Au system, Au has an fcc crystal structure with a $\bar{3}$ symmetry along the $[1\bar{1}1]$ axis, whereas MoS_2 has a hexagonal structure ($P6_3/mmc$) and is sixfold-symmetric along its [001] axis. A schematic SAED pattern of epitaxial Au on MoS_2 is shown in Fig. 1B, where the Au {220} electron-diffraction spots and the MoS_2 {110} spots are epitaxially aligned and are connected by a reciprocal lattice vector $\Delta\mathbf{g}_a$. The lattice mismatch of the parallel Au {220} planes (0.144 nm) and MoS_2 {110} planes (0.158 nm) yields a Moiré pattern with spacing $|\Delta\mathbf{g}_a|^{-1}$ equal to 1.63 nm (Fig. 1C), which can be observed in bright-field TEM images.

Design and synthesis

In this study, we attempted to synthesize ultrathin 2D Au nanodisks and examine their orientation within physically prepared bilayer MoS_2. A schematic of the synthetic process of the MoS_2-Au-MoS_2 sandwich structure is shown in Fig. 1D. First, a thin flake of MoS_2 ~50 μm in size and ~3 nm in thickness was exfoliated onto a 25-nm-thick amorphous SiN_x TEM grid using the "scotch tape" method. Next, we deposited Au onto the exfoliated MoS_2 using electron-beam evaporation with a nominal thickness set to 0.3 nm. Imaging with TEM showed that, as expected, Au formed epitaxial NPs ~3.5 nm in diameter. Afterward, the Au was physically encapsulated by a second exfoliated MoS_2 layer with orientation (θ_m) varied from 0° to 60° rotation. Optical microscope images of the sample are shown in fig. S1. Finally, we annealed the as-synthesized MoS_2-Au-MoS_2 samples between 300° and 700°C in a tube furnace in an argon (Ar) atmosphere to promote atomic rearrangement of the Au NPs between the two MoS_2 substrate layers. By plan-view TEM examination, we found that the original epitaxial Au NPs become nanodisks upon annealing and that their original epitaxial orientation (θ_a) was modified by the orientation of the upper MoS_2 layer (Fig. 1E), as determined by electron diffraction (Fig. 1F) and Moiré image analysis (Fig. 1G and fig. S2).

Synthesis of twisted epitaxial Au nanodisks

Figure 2A shows a TEM image of the MoS_2-Au-MoS_2 sample at room temperature (RT) before annealing with a bilayer twist angle θ_m equal to 19.1°. The edge of the bottom MoS_2 flake is marked in blue, and the edge of the top MoS_2 flake is marked in green, dividing the sample area into four regions: Au on the amorphous SiN_x substrate; Au on the bottom MoS_2

[1]Department of Materials Science and Engineering, Stanford University, Stanford, CA 94305, USA. [2]Materials Sciences Division, Lawrence Berkeley National Laboratory, Berkeley, CA 94305, USA. [3]Department of Applied Physics, Stanford University, Stanford, CA 94305, USA. [4]Stanford Institute for Materials and Energy Sciences, SLAC National Accelerator Laboratory, Menlo Park, CA 94025, USA. [5]Department of Energy Science and Engineering, Stanford University, Stanford, CA 94305, USA.
*Corresponding author. Email: hyhwang@stanford.edu (H.Y.H.); bobsinc@stanford.edu (R.S.); yicui@stanford.edu (Y.C.)

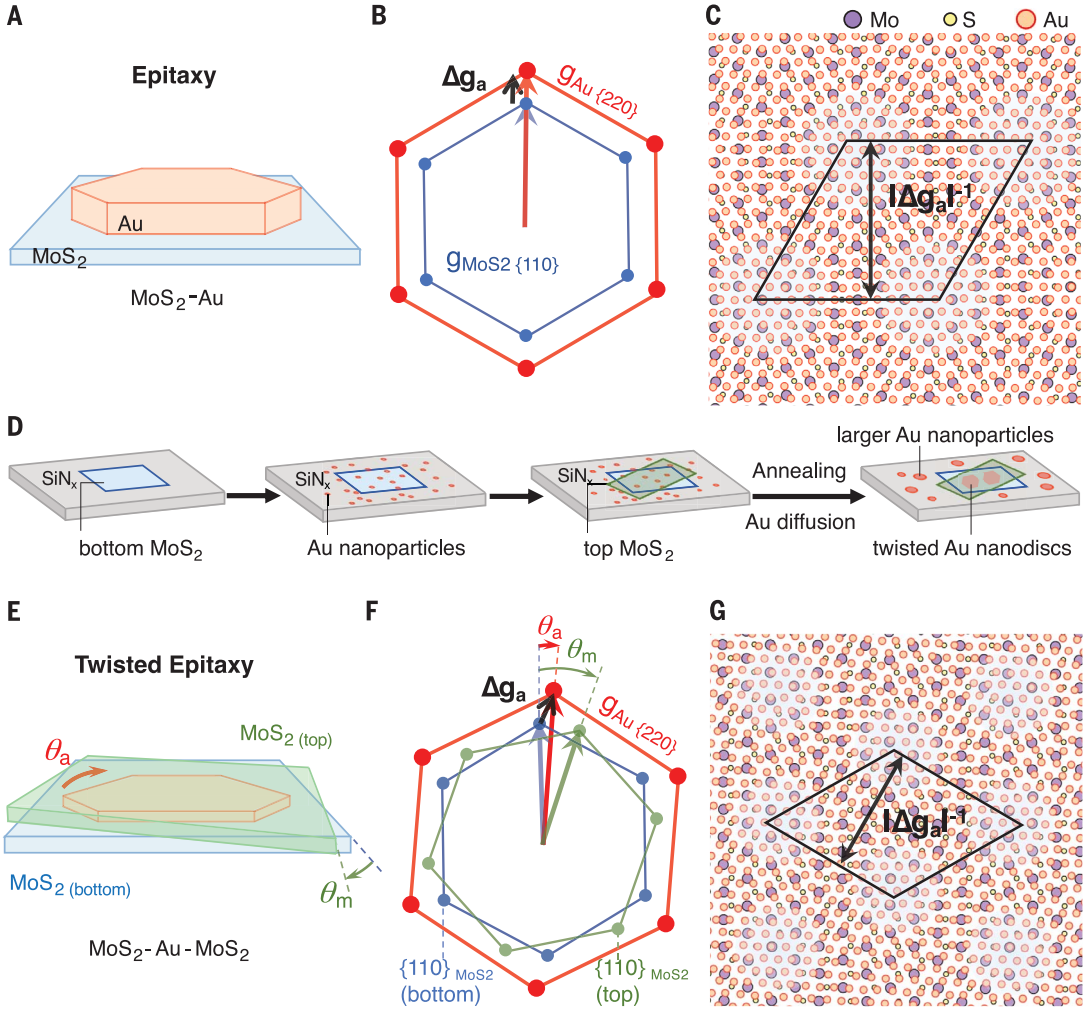

Fig. 1. Twisted epitaxial Au nanodisks. (**A**) Schematic of epitaxially aligned Au on MoS_2. (**B**) Reciprocal space model of the SAED pattern of the MoS_2-Au sample in (A). (**C**) Plan-view atomic model of 3D Au on 2D MoS_2 for Moiré patterns generated by $\Delta\mathbf{g}_a$ in (B), where $|\Delta\mathbf{g}_a|^{-1}$ notes the 3D Moiré fringe spacing. Note that we use $|\Delta\mathbf{g}_a|^{-1}$ for theoretical Moiré fringe spacing calculated from SAED patterns and *S* for Moiré fringe spacing measured from TEM images. (**D**) Schematic synthesis procedure of Au nanodisks on an amorphous silicon nitride substrate showing the physical twisting and annealing steps. (**E**) Schematic of the twisted Au nanodisks encapsulated in the vdW spacing of the bilayer MoS_2. θ_m notes the arbitrary rotation angle of the top MoS_2 relative to the bottom one. θ_a notes the twist angle of Au relative to the bottom MoS_2. (**F**) Reciprocal space model of the SAED pattern of the MoS_2-Au-MoS_2 sample in (E). (**G**) Plan-view atomic model for the Moiré patterns generated by $\Delta\mathbf{g}_a$ in (F).

(MoS_2-Au, region I); Au below the top MoS_2 (Au-MoS_2, region II); and Au encapsulated between the top and bottom MoS_2 (MoS_2-Au-MoS_2, region III). The diameter of Au NPs in regions I and III was 3.5 nm with a standard deviation of 1.2 nm, which is smaller than the NPs in region II and on the SiN_x (5.1 ± 2.6 nm). The crystal orientation of Au relative to MoS_2 was revealed by SAED. For Au on amorphous SiN_x without MoS_2 top and bottom layers, the NPs displayed random orientations (fig. S3). The SAED of Au NPs in region I (Fig. 2B) revealed epitaxial alignment with the bottom MoS_2, where {220} Au diffraction spots aligned with {110} MoS_2, which was consistent with previous studies (*42*, *43*). In region II, Au NPs on SiN_x also displayed random orientations and did not align with the top MoS_2 (Fig. 2C and fig. S4). The SAED patterns of the MoS_2-Au-MoS_2 sandwich structure (region III) (Fig. 2D) showed that Au aligned with the bottom MoS_2 layer.

To determine how the temperature affected the morphology and orientation of Au, we annealed the sample at elevated temperatures and used the results from 400° and 500°C to illustrate the changes. The schematic morphology and orientation changes of Au under different annealing conditions are given in fig. S5. The TEM image of the MoS_2-Au-MoS_2 sample after annealing in Ar at 400°C for 5 hours (Fig. 2E) shows that the Au NPs on SiN_x and in region I underwent Ostwald ripening and grew larger (10.4 ± 4.5 nm), whereas Au NPs in regions II and III remained small (3.7 ± 1.2 nm). The SAED of the four regions showed that the Au on SiN_x remained randomly orientated, and that Au in region I was still aligned with the bottom MoS_2 (Fig. 2F). The Au in region II epitaxially aligned with the top MoS_2, where {220} Au spots were aligned with {110} MoS_2 spots (Fig. 2G, inset). In region III, {220} planes of Au epitaxially aligned with the {110} planes of bottom MoS_2 (Fig. 2H, bottom-right inset), whereas no epitaxial diffraction spots of {220} Au were observed aligned with the top {110} MoS_2 spot (Fig. 2H, top-right inset). These results indicate that the interaction of Au with the top MoS_2 was weaker than that with the bottom one (Fig. 2H).

After annealing the sample in Ar at 500°C for 2 hours (Fig. 2I), Au nanodisks with an average diameter of ~50 nm were observed as larger, less dark contrast regions around the edge of the sandwiched region III. In regions I and II, the Au NPs grew slightly larger, but no Au nanodisks were observed in these two regions (fig. S6). The presence of Au was confirmed by energy-dispersive x-ray spectroscopy (EDS; fig. S7), and the disk morphology was verified by sample tilting (fig. S8). The SAED patterns of regions I and II are shown in Fig. 2, J and K, respectively. The intensity of {220} Au spots became stronger compared with those after annealing at 400°C in both regions and retained epitaxial alignment with the {110} MoS_2 spots. The SAED pattern of Au nanodisks in region III is shown in Fig. 2L, where the bilayer twist angle θ_m was determined to be unchanged after annealing. The orientation of Au {220} planes still matches closely with that of the bottom MoS_2 {110} planes. However,

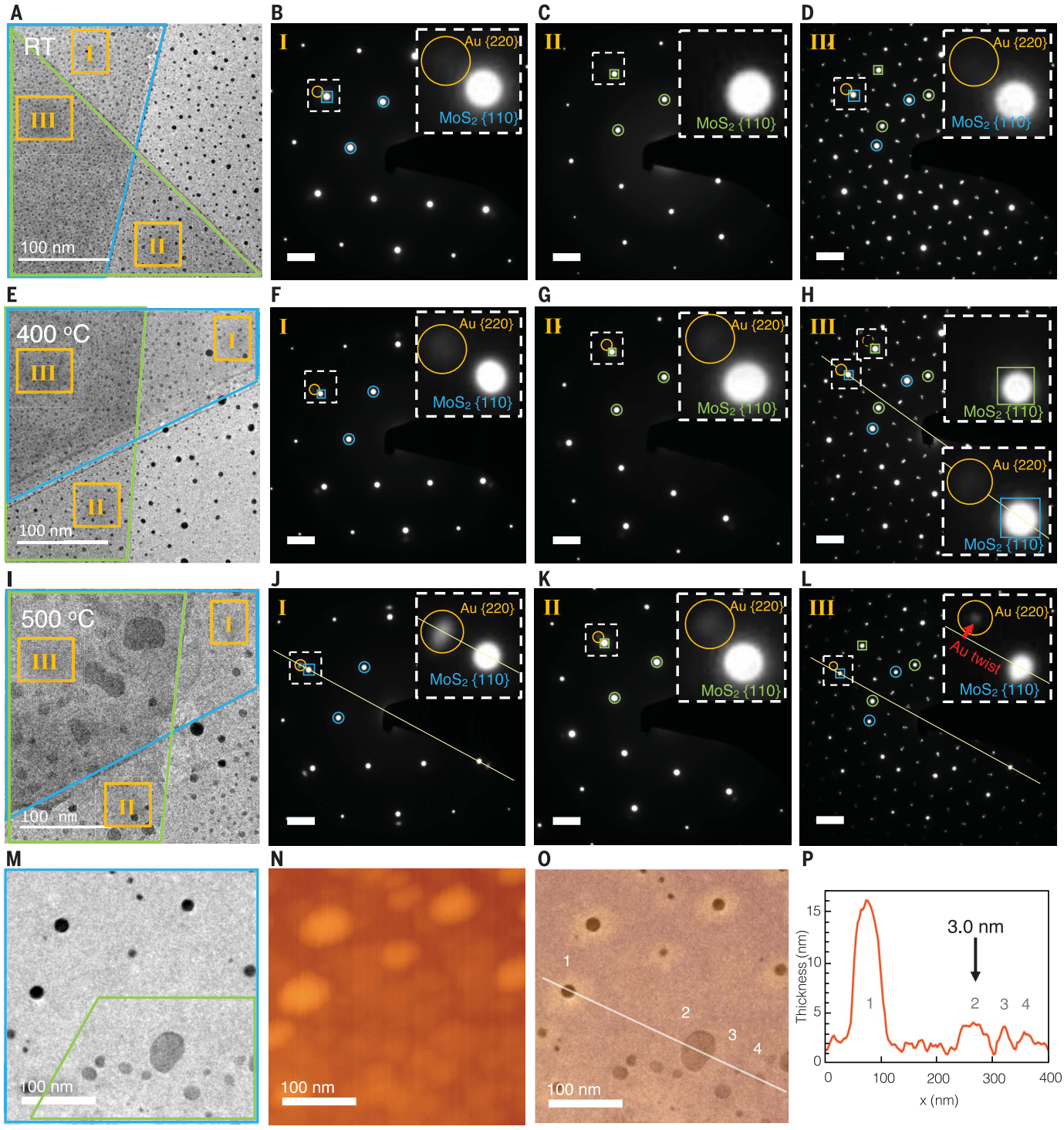

Fig. 2. Synthesis, alignment, and thickness of Au nanodisks. (**A**) Bright-field TEM image of a freshly prepared MoS_2-Au-MoS_2 sample on a 25-nm-thick SiN_x membrane showing the Au nanoparticles as dark on a bright background. The edges of the top and bottom MoS_2 are marked in green and blue, respectively. (**B** to **D**) The SAED patterns of regions I, II, and III in (A), respectively. The diameter of the selected area was about 200 nm. The insets have the same orientation as the smaller boxed regions, and they show the epitaxial alignment of Au {220} diffraction spots with MoS_2 {110} spots. Scale bars: 2 nm^{-1}. (**E**) Bright-field TEM image of MoS_2-Au-MoS_2 sample after annealing in Ar at 400°C for 5 hours. (**F** to **H**) The SAED patterns of regions I, II, and III in (E), respectively, showing the epitaxial alignment of Au {220} diffraction spots with MoS_2 {110} spots. Scale bars: 2 nm^{-1}. (**I**) Bright-field TEM image of MoS_2-Au-MoS_2 sample after annealing in Ar at 500°C for 2 hours. (**J** to **L**) The SAED patterns of regions I, II, and III in (I), respectively. The yellow lines in (H), (J), and (L), drawn radially, note the ideal alignment. Scale bars: 2 nm^{-1}. (**M** to **P**) Thickness measurement of Au nanodisks. (M) Bright-field TEM image of Au nanodisks (gray particles) and Au nanoballs (dark particles). The edges of the top and bottom MoS_2 are marked in green and blue, respectively. (N) AFM image of the same region as in (M). (O) Superposition of (M) and (N), indicating the position of Au nanodisks relative to Au nanoballs. (P) Thickness profile of four NPs in (O), where the thickness of nanodisk 2 is 3 nm, and the thickness of nanodisks 3 and 4 is 2 nm.

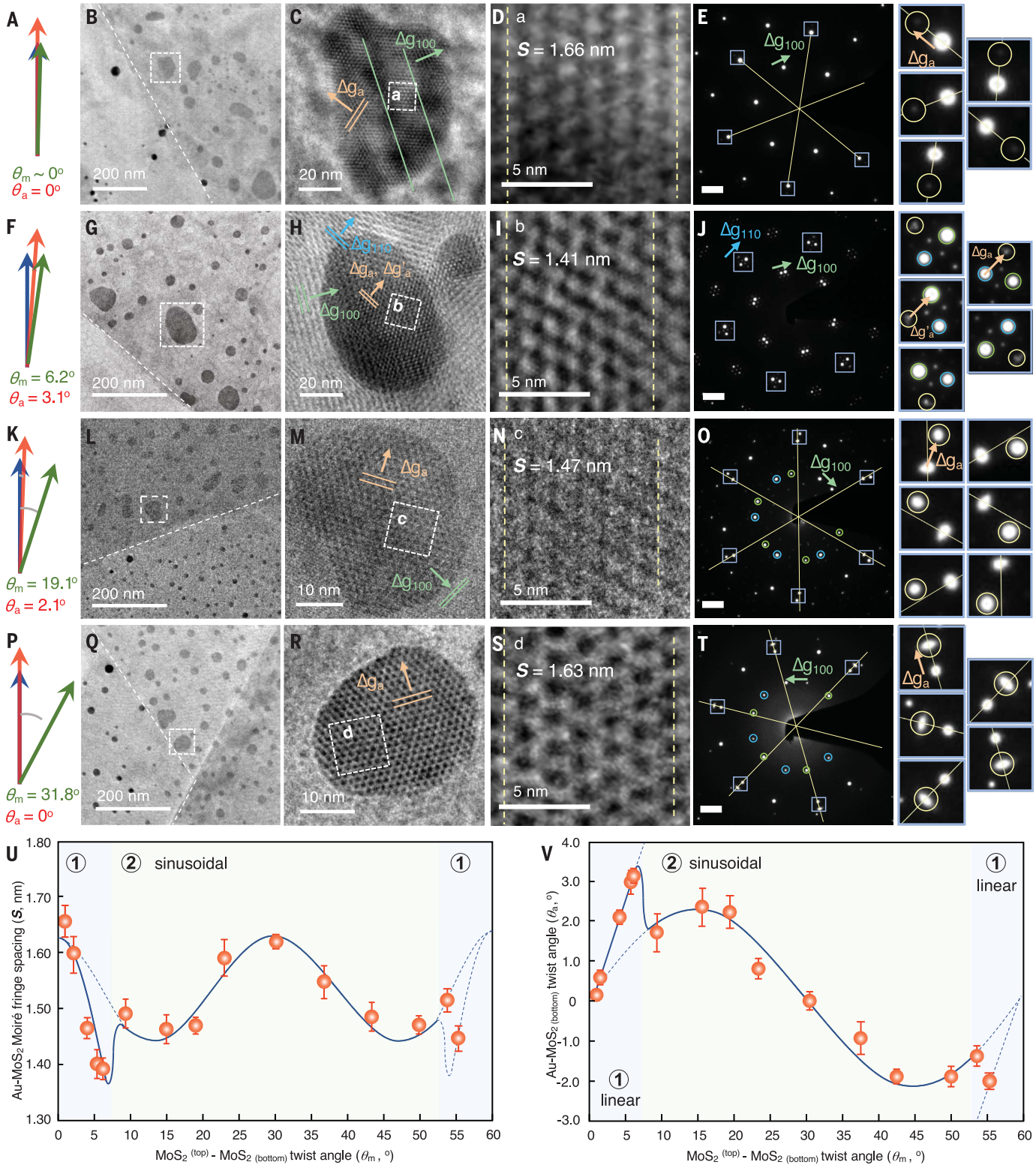

Fig. 3. MoS_2 rotation angle–dependent twist of Au nanodisks. (**A**) Schematic reciprocal lattice orientation of Au and the top and bottom MoS_2 in (B) with a small bilayer twist angle θ_m = 0.8°. The red arrow notes the reciprocal lattice vector of the Au {220} planes, and the green and blue arrows are reciprocal lattice vectors of the {110} planes of the top and bottom MoS_2, respectively. (**B**) Bright-field TEM image of MoS_2-Au-MoS_2. A white dashed line denotes the edge of the top MoS_2. (**C**) Bright-field TEM image of a typical Au nanodisk marked with a white dashed box in (B). Green lines indicate the Moiré fringes with spacing equal to 20.1 nm originating from the top and bottom MoS_2. Orange lines indicate the Moiré fringes originate from Au and the bottom MoS_2. (**D**) Higher magnification zoom-in image of region "a" marked in the white dashed box in (C), showing the smaller-spacing Moiré fringes. (**E**) SAED pattern of MoS_2-Au-MoS_2 in (B). $\Delta\mathbf{g}_a$ and $\Delta\mathbf{g}_{100}$ note the vectors that generate Moiré fringes from the Au-bottom MoS_2 and from the {100} planes of the bilayer MoS_2, respectively. Yellow lines show the ideal alignment

of Au with the bottom MoS_2. Scale bars: 2 nm^{-1}. (**F** to **T**) MoS_2-Au-MoS_2 samples with θ_m = 6.2°, 19.1°, and 31.8°, respectively. When θ_m = 6.2°, Au reorients to halfway between the bilayer MoS_2. When θ_m = 19.1°, Au aligns closely with the bottom MoS_2 layer, with misalignment θ_a determined to be 2.1°. When θ_m = 31.8°, Au epitaxially aligns with the bottom MoS_2 layer. Scale bar in SAED patterns: 2 nm^{-1}. $\Delta\mathbf{g'}_a$ and $\Delta\mathbf{g}_{110}$ note the vectors that generate Moiré fringes from the Au-top MoS_2 and the {110} planes of the bilayer MoS_2, respectively. (**U**) The relationship between the Moiré spacing from Au and the lower MoS_2 (*S*) and the rotation angle of the top and bottom MoS_2 (θ_m). (**V**) The relationship between the twist angle of Au relative to the bottom MoS_2 (θ_a) and the rotation angle of the top and bottom MoS_2 (θ_m) as determined from the diffraction patterns, showing two separate regions. Note that the Moiré spacings are ambiguous with respect to the direction of the twist, although their orientations (perpendicular to $\Delta\mathbf{g}^{-1}$) are not. The error bars in our analysis represent the standard deviation of the small difference of diffraction spot positions in the selected area diffraction patterns (fig. S30).

small deviations from the ideal epitaxy were observed, with θ_a determined to be 2.0° in the same direction as θ_m in this case (Fig. 2L, inset). The Au in region I was not twisted (Fig. 2J), which indicated that the top layer was necessary for change in Au orientation. We note that Au in region III was not twisted after annealing at 400°C (Fig. 2H), indicating that Au only reoriented during the nanodisk evolution at 500°C. The {220} lattice spacing of Au nanodisks was determined to be 0.144 nm from the SAED pattern (fig. S19), consistent with the natural lattice parameter of Au.

The thickness of Au nanodisks was measured separately using atomic force microscopy (AFM). The TEM and AFM images of the same Au nanodisks encapsulated in the bilayer MoS_2 are shown in Fig. 2, M and N, respectively (the AFM lateral resolution was not as high as that of the TEM images in this case). Figure 2O shows the superposition of the TEM and AFM images, in which the brighter regions (higher protrusions) in the AFM image matched well with the large dark Au NPs in the TEM image. The height of the large Au NP in region I (labeled "1") was determined to be 15.5 nm, which was similar to its diameter (15.2 nm) measured from the TEM image (fig. S9). These results show that the NP remained approximately spherical, consistent with tilting results (fig. S8). The thickness of the Au nanodisks in the sandwich region III (labeled "2," "3," and "4") was measured and found to be between 2 and 3 nm (Fig. 2P). Note that the nominal thickness of Au here was set to 0.3 nm in the electron-beam evaporation. Figure S10 shows the samples where the nominal thickness of Au was 1.0 and 0.1 nm. Au nanodisks were not formed in the former sample, whereas smaller (~6.6 nm in diameter) and thinner (~1.0 nm in thickness) Au nanodisks are observed in the latter sample compared with the case when the Au nominal thickness was 0.3 nm.

Orientation of twisted epitaxial Au nanodisks

To understand further how the top MoS_2 affected the orientation of Au nanodisks annealed at 500°C and the Moiré fringes originating from the overlapping crystals in the TEM images, we correlated the Moiré pattens and the SAED patterns from a series of samples with different MoS_2 bilayer twist angles ($0° < \theta_m < 60°$) (Fig. 3). Figure 3A shows the schematic reciprocal lattice orientation of the top MoS_2, Au, and the bottom MoS_2, where the MoS_2 twist angle θ_m is 0.8° and the Au orientation θ_a is 0°. The bright-field TEM image is shown in Fig. 3B. A typical Au nanodisk (marked with a white dashed square in Fig. 3B and shown in higher magnification in Fig. 3C) had an average Moiré fringe spacing of Au and the bottom MoS_2 (*S*) of 1.66 nm (Fig. 3D). This value is near the theoretical spacing from the parallel lattice planes, indicating that the Au was not twisted in this case (fig. S18). This finding was further confirmed by the diffraction pattern (Fig. 3E, insets), as Au {220} spots were epitaxially aligned with MoS_2 {110} spots.

Figure 3, F to T, shows the samples with bilayer MoS_2 twist angles θ_m = 6.2°, 19.1°, and 31.8°. Au nanodisks with a diameter of ~50 nm were found in each case. In the case where θ_m = 6.2°, θ_a was determined to be 3.1°, indicating that the Au reoriented midway between the top and bottom MoS_2 orientations. As shown in Fig. 3H, three sets of Moiré fringes coexist in this system, which are perpendicular to their corresponding reciprocal lattice vectors noted in the diffraction pattern. In Fig. 3J, the Au {220} spots overlap with double diffraction spots from the bilayer MoS_2. The double diffraction effect were reduced to make the Au diffraction spots clearer by slightly tilting the sample (fig. S14A). When θ_m = 19.1°, Au {220} planes matched closely with the lower MoS_2 {110} planes with a smaller misalignment θ_a determined to be 2.1° (Fig. 3O). When θ_m = 31.8° (near 30°), the Au nanodisks epitaxially aligned with the bottom MoS_2 again (Fig. 3T). The Au diffraction spots were round circles when θ_m was 0° and 19.1° but were elongated in the tangential direction when θ_m was 6.2° and 31.8°.

Figure 3, I, N, and S, shows the magnified images of the Moiré fringes from the Au nanodisks and bottom MoS_2 layer, from which *S* was measured to be 1.41, 1.47, and 1.63 nm, respectively, offering direct evidence that the Moiré spacings changed in response to the Au twist. The bright-field TEM images and SAED patterns of all the other samples with different θ_m are shown in figs. S11 to S13. Note that in most instances, Au nanodisks only evolved at the edge within about 600 nm of the sandwich region. This spatial effect might be the result of the confinement of Au at the peripheral area of the bilayer being lower than that at the central area, which would favor Au diffusion (fig. S15). Increasing the annealing temperature and annealing time extended the width of the edge region by about three to four times (fig. S16). A larger-scale synthesis of Au nanodisks could be achieved by patterning (fig. S17).

The experimentally observed *S*, θ_a, and θ_m were highly correlated, as expected. In Fig. 3U, we plot the *S* measured from TEM images versus θ_m over a 60° range. Figure 3V shows the relationship between θ_a, measured from the diffraction pattern, and θ_m. The results show two separate parts. At first, up to about θ_m = 7°, θ_a increased linearly with θ_m with θ_a = 1/2 θ_m. Above θ_m = 7°, θ_a varied approximately sinusoidally with θ_m and roughly followed a variation $\theta_a = 2.2 \sin(6\theta_m)$. The plot of *S* versus θ_a is shown in fig. S18. The data follow the theoretical relationship $S = d_m d_a / [(d_m - d_a)^2 + d_m d_a \theta_a^2]^{1/2} = |\Delta\mathbf{g}_a|^{-1}$ (*45*), indicating that the Au twist solely contributed to the Moiré spacings and orientation changes. To further confirm that there was no associated lattice spacing change, we measured the diffraction spot positions of MoS_2 {110} and Au {220} in the SAED patterns (fig. S19). Both displayed lattice strains smaller than 1%.

The intermediate strength of S–Au atomic interaction is thought to be possibly important for the Au anisotropic coupling and nanodisk evolution. For a brief examination of this point, we changed our template from MoS_2 to graphene, for which there is a much weaker C–Au interaction. After annealing at 500°C for 2 hours in Ar, Au nanodisks were found in MoS_2-Au-graphene and graphene-Au-MoS_2, where graphene replaced the top and bottom layer MoS_2 in MoS_2-Au-MoS_2, respectively (fig. S20). In both cases, Au only epitaxially aligned with MoS_2, regardless of the bilayer twist angle. In addition, no Au nanodisks were observed in bilayer graphene (figs. S21 to S23). Therefore, a strong interaction from one interface with Au is necessary for nanodisk evolution, and the interactions from both interfaces are important for the reorientation of the Au nanodisks.

Density functional theory calculations

The orientation preference of twisted epitaxial Au in the twisted bilayer MoS_2 is most likely associated with a lowering of the sum of the two interfacial energies of MoS_2-Au-MoS_2. We define the interfacial energy of Au with the top

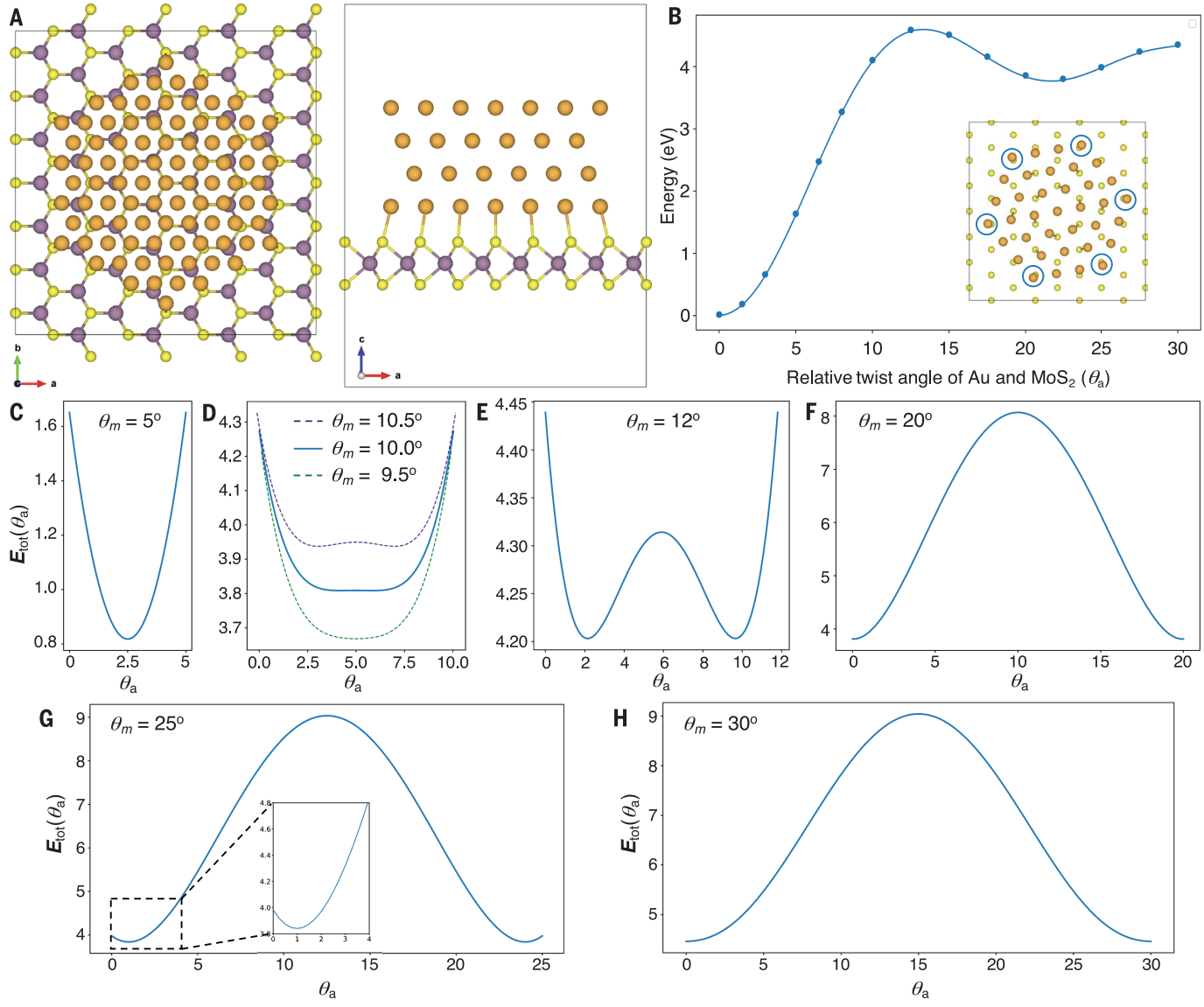

Fig. 4. DFT calculations. (**A**) Schematic configuration of four $(1\bar{1}1)$ planes of Au on a monolayer MoS_2 with 0° rotation. Orange, purple, and yellow balls represent Au, Mo, and S atoms, respectively. (**B**) Calculated energy of the MoS_2-Au model as a function of the relative twist angle of Au and MoS_2 (θ_a) showing a global minimum at θ_a = 0° and a local minimum at θ_a ~ 20°. The inset shows the MoS_2-Au structure with relative twist angle at 20°. Approximate coincidence sites are marked with blue circles. Mo atoms and three Au layers are omitted. (**C** to **H**) Total interfacial energy (E_{tot}, electron volts) of MoS_2-Au-MoS_2 as a function of θ_a (degrees) at different bilayer MoS_2 twist angles (θ_m, degrees) as obtained from fitting the DFT data in (B). (C) When θ_m = 5°, E_{tot} displays a minimum at θ_a = 2.5°. (D) Symmetry breaking of E_{tot} when θ_m ~ 10°. (E) E_{tot} displays two minima at θ_a ~ 2° and θ_a ~ 10° when θ_m = 12°. (F) E_{tot} displays two minima at θ_a = 0° and θ_a = 20° when θ_m = 20°. (G) E_{tot} displays two minima at θ_a ~ 1° and θ_a ~ 24° when θ_m = 25°. The inset is the magnified image of the plot clearly showing the minimum at θ_a ~ 1°. (H) E_{tot} displays two minima at θ_a = 0° and θ_a = 30° when θ_m = 30°, consistent with the MoS_2-Au crystallography.

MoS_2 as E_{top} and the interfacial energy of Au with the bottom MoS_2 as E_{bottom}, and we approximate the total interfacial energy E_{tot} as the sum of E_{top} and E_{bottom}

$$E_{tot} = E_{top} + E_{bottom}$$

For a certain θ_m, the orientation mismatch of Au with the bottom MoS_2 is defined as θ_a, and the orientation mismatch of Au with the top MoS_2 is $\theta_m - \theta_a$. Assuming that E_{top} and E_{bottom} can be described by the same function $E_{interfacial}(\theta_a)$, as they are both Au-$MoS_2$ contacts, E_{tot} becomes a function of θ_a

$$E_{tot}(\theta_a) = E_{interfacial}(\theta_a) + E_{interfacial}(\theta_m - \theta_a)$$

We performed density functional theory (DFT) calculations on a MoS_2-Au model system to find $E_{interfacial}$ as a function of θ_a (see methods in the supplementary materials). Figure 4A shows the plan view and side view of this structure with Au epitaxially aligned with MoS_2. Other configurations were obtained by rotating the Au layers in steps of 1.5° from 0° to 30° relative to the epitaxial configuration with the MoS_2 layer. The calculated energy of Au and MoS_2 with different twist angles is plotted in Fig. 4B. Note that the output energy in DFT is the total energy for the whole structure, which is not the interfacial energy of the Au-MoS_2 interface. However, as the relative twist angle is the only variable in this Au-MoS_2 structure, we choose the total energy of zero twist angle as the reference for $E_{interfacial}$ (θ_a). The interfacial energy is lowest at the epitaxial

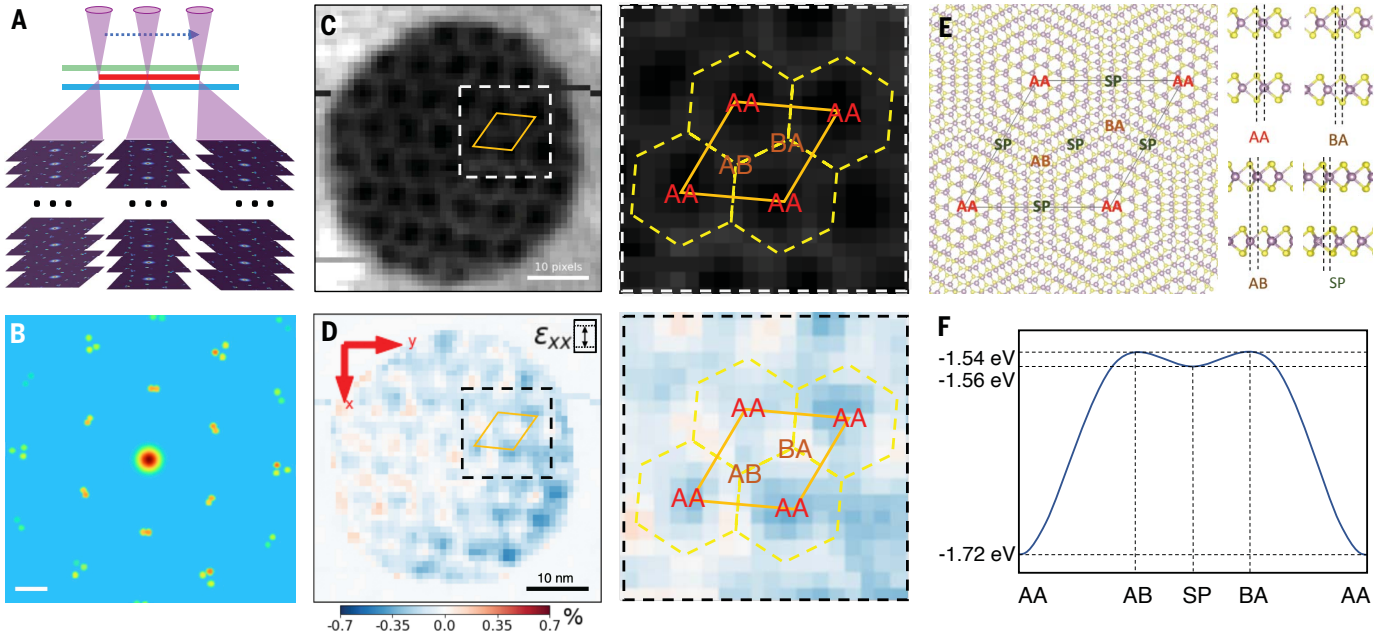

Fig. 5. 4D-STEM strain analysis. (**A**) Schematic of 4D-STEM showing scanning convergent beam (purple) and corresponding diffraction patterns at each point. Green, red, and blue lines represent top MoS_2, Au, and bottom MoS_2, respectively. (**B**) Diffraction pattern of MoS_2-Au-MoS_2 sample showing θ_m = 3.5° and θ_a = 1.7°. Scale bar: 2 nm^{-1}. (**C**) Virtual bright-field image reconstructed using MoS_2 {100} diffraction spots and the transmitted beam spot showing Au (dark area) encapsulated in bilayer MoS_2 (whole area) and bilayer Moiré pattern with a 5.5-nm period. Pixel size: 1 nm. Scare bar: 10 nm. The magnified image shows the bilayer Moiré pattern (yellow dashed hexagon) and Moiré supercell (orange diamond). As there is one AA stacking, two AB/BA stackings, and three SP stackings in one Moiré supercell, the AA, AB/BA, and SP stacking regions are determined by comparing the TEM image with the atomic model in (E), which is also confirmed by multislice simulation (fig. S31). (**D**) Uniaxial strain ε_{xx} map of Au, showing small periodic strain (<|±0.5%|) in Au with a 5.5-nm period and a compressive strain of Au at AA stacking. The lattice parameter of Au measured from SAED pattern was chosen as a reference for zero strain, as it indicates the average lattice parameter of Au. (**E**) Atomic structure of the Moiré supercell of twisted bilayer MoS_2 with a twist angle of 6°, showing AA, AB, BA, and SP stacking configurations. (**F**) Calculated interaction energy of Au with the twisted bilayer at different stacking configurations using DFT, showing that the interaction energy between a single Au atom and the twisted bilayer MoS_2 at AA stacking is ~170 meV lower than that at AB/BA and SP stacking.

position and increases for all the other values. At small relative twist angles, the interfacial energy appears as a convex function. There is a local minimum of $E_{interfacial}$ (θ_a) at ~20° that we attribute to the formation of a relatively high areal density of approximate coincidence sites of Au and S atoms (Fig. 4B, inset).

Figure 4, C to H, shows the plots of E_{tot} (θ_a) with different θ_m. When θ_m is small (θ_m = 5°), given the convex nature of interfacial energy at small relative twist angle, E_{tot} (θ_a) displays only one minimum at θ_a = 1/2 θ_m, which is consistent with the reorientation results (Fig. 4C). Figure 4D shows that when θ_m increases from 9.5° to 10.5°, E_{tot} (θ_a) first displays a single energy minimum at θ_a ~ 5° and then quickly bifurcates to two local minima at θ_a ~ 2.5° and θ_a ~ 7.5°, which explains the rapid change of θ_a between the linear and sinusoidal region in Fig. 3V. Au always couples closely with the bottom MoS_2 but not the top one because, in the initial state (before annealing), Au always epitaxially aligns with the bottom layer. The increase of the energy barrier at 1/2 θ_m impedes the Au coupling with the top MoS_2 (Fig. 4E).

When θ_m increases to 20°, 25°, and 30°, the energy barrier becomes higher and pushes the energy minimum position of E_{tot} (θ_a) to be around θ_a = 0°, 1°, and 0°, respectively (Fig. 4, F to H). The simulation results are consistent with the experimental observations overall, except when θ_m is around 20°. In this case, the calculations predict no Au reorientation while a 2° rotation exists in the experiment, which might be due to the difference between the simulation model and the real sample (fig. S24). For example, a set of screwlike interface dislocations (analogous to those in low-angle twist grain boundaries) may need to be taken into account for the interface energies in the low-twist regime, as they may be present in the real system. We envision that such twisted epitaxial relationship could happen in other 2D systems when their interfacial energy is a convex function at a small twist angle regime but may not happen if the interfacial energy is a concave function.

4D-STEM strain analysis

The strain variations in the Au nanodisks associated with the twisted epitaxy were studied using 4D scanning transmission electron microscopy (4D-STEM) (*46*). The schematic 4D-STEM experiment is shown in Fig. 5A, where a focused electron beam with a convergence semi-angle of 0.4 mrad was rastered across an Au nanodisk encapsulated in twisted bilayer MoS_2 with a step size of 1 nm, and the diffracted electron signal was collected at each probe position. The resulting diffraction pattern is shown in Fig. 5B, from which θ_m and θ_a are determined to be 3.5° and 1.7°, respectively, illustrating the twisted epitaxial alignment of Au.

Virtual bright-field and virtual annular dark-field images of the sample reconstructed from the diffraction pattern revealed the Moiré pattern of bilayer MoS_2 with a period of 5.5 nm, corresponding to the bilayer twist angle (Fig. 5C and fig. S25). Lattice spacing maps of Au {440} planes and $\{\bar{2}24\}$ planes revealed a periodic lattice spacing change with the same period as the bilayer Moiré pattern (fig. S26). Further strain analysis (uniaxial strain ε_{xx} and ε_{yy}, shear strain ε_{xy}, and rotation θ) confirmed the existence of a small periodic strain variation (<|±0.5%|) in Au with the same period as the bilayer Moiré pattern (Fig. 5D and fig. S27). This periodic strain of Au was most likely associated with the different chemical environment of Au at different stacking configurations [AA, AB, BA, and saddle point (SP)] of twisted bilayer MoS_2 (Fig. 5E).

The uniaxial strain (ε_{xx}) map of Au (Fig. 5D) revealed compressive strain of Au at the AA stacking region of bilayer MoS_2, as well as a small tensile strain of Au at the AB stacking (fig. S27A), which we qualitatively corroborated using DFT calculations (fig. S28). The interaction energy between a single Au atom and the twisted bilayer MoS_2 at the AA stacking region was calculated to be ~170 meV lower than that at the AB or SP stacking region (Fig. 5F). This result indicated that the twisted bilayer MoS_2 exerted a periodic potential on Au with a potential well around the AA region ~170 meV deeper than that at AB or SP, resulting in the confinement of Au at the AA region and thus a compressed strain. Further 4D-STEM analysis showed that, when the twist angle of the bilayer MoS_2 reached a relatively large value, such as 12°, which corresponded to a bilayer Moiré pattern of 1.33 nm, the strain of Au nanodisks encapsulated in the bilayer was negligible (fig. S29).

Discussion

The discovery of twisted epitaxial structure of Au and MoS_2 presents possibilities for structure-function investigation of 2D materials with advanced electron microscopy. The TEM Moiré pattern images are representations of the atomic matching and mismatching of the participating crystals. The periodicity is directly associated with the atomic matching of the two materials, changes of which (as demonstrated here) are likely to influence the composite physical properties, such as the band structure (*47*), electronic and optical properties of Au and MoS_2 [plasmon-exciton plexciton (*48*)], etc. Moreover, twisted epitaxy implies the possibility of using the van der Waals spacing of the stacked bilayer 2D material as a nanoreactor to confine material growth and tune the crystal morphology, orientation, and lattice strain, indicating that the bilayer orientation can act as an additional parameter to control the structure and properties of the encapsulated atoms.

REFERENCES AND NOTES

1. A. Y. Cho, J. R. Arthur, *Prog. Solid State Chem.* **10**, 157–191 (1975).
2. M. B. Panish, *Science* **208**, 916–922 (1980).
3. D. C. Tsui, H. L. Stormer, A. C. Gossard, *Phys. Rev. Lett.* **48**, 1559–1562 (1982).
4. S. Nakamura, *Jpn. J. Appl. Phys.* **30**, L1705–L1707 (1991).
5. X. Peng, M. C. Schlamp, A. V. Kadavanich, A. P. Alivisatos, *J. Am. Chem. Soc.* **119**, 7019–7029 (1997).
6. B. O. Dabbousi *et al*., *J. Phys. Chem. B* **101**, 9463–9475 (1997).
7. S. E. Habas, H. Lee, V. Radmilovic, G. A. Somorjai, P. Yang, *Nat. Mater.* **6**, 692–697 (2007).
8. O. Chen *et al*., *Nat. Mater.* **12**, 445–451 (2013).
9. L. J. Lauhon, M. S. Gudiksen, D. Wang, C. M. Lieber, *Nature* **420**, 57–61 (2002).
10. Y. Wu, J. Xiang, C. Yang, W. Lu, C. M. Lieber, *Nature* **430**, 61–65 (2004).
11. T. Mårtensson *et al*., *Nano Lett.* **4**, 1987–1990 (2004).
12. W. W. Hooper, W. I. Lehrer, *Proc. IEEE* **55**, 1237–1238 (1967).
13. C. Thelander *et al*., *Mater. Today* **9**, 28–35 (2006).
14. J. Xiang *et al*., *Nature* **441**, 489–493 (2006).
15. J. Goldberger, A. I. Hochbaum, R. Fan, P. Yang, *Nano Lett.* **6**, 973–977 (2006).
16. S. Nakamura, T. Mukai, M. Senoh, *Appl. Phys. Lett.* **64**, 1687–1689 (1994).
17. A. Tsukazaki *et al*., *Nat. Mater.* **4**, 42–46 (2005).
18. R. Yan, D. Gargas, P. Yang, *Nat. Photonics* **3**, 569–576 (2009).
19. S. Nakamura *et al*., *Jpn. J. Appl. Phys.* **35**, L74–L76 (1996).
20. W. Tsang, *IEEE J. Quantum Electron.* **20**, 1119–1132 (1984).
21. X. Duan, Y. Huang, R. Agarwal, C. M. Lieber, *Nature* **421**, 241–245 (2003).
22. S. Gandrothula, T. Kamikawa, J. S. Speck, S. Nakamura, S. P. DenBaars, *Appl. Phys. Express* **14**, 031002 (2021).
23. M. T. Björk *et al*., *Appl. Phys. Lett.* **81**, 4458–4460 (2002).
24. M. Law, J. Goldberger, P. Yang, *Annu. Rev. Mater. Res.* **34**, 83–122 (2004).
25. M. Gurioli, Z. Wang, A. Rastelli, T. Kuroda, S. Sanguinetti, *Nat. Mater.* **18**, 799–810 (2019).
26. T. Kanne *et al*., *Nat. Nanotechnol.* **16**, 776–781 (2021).
27. Y. Gong *et al*., *Nat. Mater.* **13**, 1135–1142 (2014).
28. Y. Shi *et al*., *Nano Lett.* **12**, 2784–2791 (2012).
29. Z. Chen *et al*., *Sci. Adv.* **7**, eabk0115 (2021).
30. K. Reidy *et al*., *Nat. Commun.* **12**, 1290 (2021).
31. Y. Kim *et al*., *Nature* **544**, 340–343 (2017).
32. H. Kim *et al*., *ACS Nano* **2**, 40 (2022).
33. A. E. White, K. T. Short, R. C. Dynes, J. P. Garno, J. M. Gibson, *Appl. Phys. Lett.* **50**, 95–97 (1987).
34. T. George, R. W. Fathauer, *Appl. Phys. Lett.* **59**, 3249–3251 (1991).
35. N. Briggs *et al*., *Nat. Mater.* **19**, 637–643 (2020).
36. G. Algara-Siller *et al*., *Nature* **519**, 443–445 (2015).
37. Q. Yang *et al*., *Nature* **588**, 250–253 (2020).
38. K. Mustonen *et al*., *Adv. Mater.* **34**, e2106922 (2022).
39. Z. Y. Al Balushi *et al*., *Nat. Mater.* **15**, 1166–1171 (2016).
40. B. Pécz *et al*., *Adv. Mater.* **33**, e2006660 (2021).
41. A. Allain, J. Kang, K. Banerjee, A. Kis, *Nat. Mater.* **14**, 1195–1205 (2015).
42. I. Popov, G. Seifert, D. Tománek, *Phys. Rev. Lett.* **108**, 156802 (2012).
43. K. Reidy *et al*., *Nano Lett.* **22**, 5849–5858 (2022).
44. M. H. Jacobs, M. J. Stowell, *Philos. Mag.* **11**, 591–603 (1965).
45. D. B. Williams, C. B. Carter, *Transmission Electron Microscopy: A Textbook for Materials Science* (Springer, 2009).
46. C. Ophus, *Microsc. Microanal.* **25**, 563–582 (2019).
47. S. Forti *et al*., *Nat. Commun.* **11**, 2236 (2020).
48. A. B. Yankovich *et al*., *Nano Lett.* **19**, 8171–8181 (2019).
49. Y. Cui *et al*., Twisted epitaxy of gold nanodisks grown between twisted substrate layers of molybdenum disulfide [Dataset], Dryad (2023); https://doi.org/10.5061/dryad.wpzgmsbv3.

ACKNOWLEDGMENTS

We acknowledge the use and support of the Stanford Nano Shared Facilities (SNSF). Part of this work was performed at SNSF, partially supported by the National Science Foundation under award ECCS-1542152. We also acknowledge helpful discussions of 4D-STEM data analysis with C. Ophus at the National Center for Electron Microscopy at the Molecular Foundry, Lawrence Berkeley National Laboratory. **Funding:** This work was supported by the Office of Basic Energy Sciences, US Department of Energy, Division of Materials Science and Engineering, DE-AC02-76SF00515. **Author contributions:** Conceptualization: Y.C. (first author) and Y.C. (corresponding author). Sample preparation: Y.C. (first author), Y.W., and Y.L. TEM characterization: Y.C. (first author) and R.S. AFM characterization: Y.C. (first author). DFT calculations: Y.C. (first author), J.W., and E.B. 4D-STEM: Y.C. (first author) and R.S. Discussion: W.Z., Z.Z., and J.Z. Writing – original draft: Y.C. (first author). Writing – review & editing: H.Y.H., R.S., and Y.C. (corresponding author). **Competing interests:** The authors declare that they have no competing interests. **Data and materials availability:** All data needed to evaluate the conclusions in this paper are present in the main text or the supplementary materials. Codes that support the plots within this paper are available at Dryad (*49*).

SUPPLEMENTARY MATERIALS

science.org/doi/10.1126/science.adk5947
Materials and Methods
Supplementary Notes
Figs. S1 to S31
References (*50*–*57*)

Submitted 30 August 2023; accepted 27 November 2023
10.1126/science.adk5947

Twisted epitaxy of gold nanodisks grown between twisted substrate layers of molybdenum disulfide

Yi Cui, Jingyang Wang, Yanbin Li, Yecun Wu, Emily Been, Zewen Zhang, Jiawei Zhou, Wenbo Zhang, Harold Y. Hwang, Robert Sinclair, and Yi Cui

Science **383** (6679), . DOI: 10.1126/science.adk5947

Editor's summary

Epitaxial growth of a crystalline film normally proceeds from one substrate. Cui *et al*. report that two molybdenum disulfide (MoS_2) layers can both impose orientation effects on gold. The authors grew gold nanoparticle layers on one MoS_2 substrate and then covered the nanoparticles with a second MoS_2 film. Upon heating, the nanoparticles flattened to nanodisks. For small twist angles between the two substrates (about 7 degrees), the nanometer-thick gold nanodisks adopted an orientation intermediate to both substrates. This alignment was driven in part by the chemical interaction of gold with sulfur. —Phil Szuromi